This is a preprint version.
Published in Combustion Theory and Modelling (2017)
DOI: 10.1080/13647830.2017.1349343

Three-step approach for prediction of limit cycle pressure oscillations in combustion chambers of gas turbines

Dmytro Iurashev[a]*, Giovanni Campa[b], Vyacheslav V. Anisimov[b] and Ezio Cosatto[b]

[a]*Università degli Studi di Genova, DICCA, Genoa, Italy;* [b]*R&D/Combustor, Ansaldo Energia S.p.A., Genoa, Italy*

(*Received 17 August 2016; accepted 15 June 2017*)

Currently, gas turbine manufacturers frequently face the problem of strong acoustic combustion driven oscillations inside combustion chambers. These combustion instabilities can cause extensive wear and sometimes even catastrophic damages to combustion hardware. This requires prevention of combustion instabilities, which, in turn, requires reliable and fast predictive tools. This work presents a three-step method to find stability margins within which gas turbines can be operated without going into self-excited pressure oscillations. As a first step, a set of unsteady Reynolds-averaged Navier–Stokes simulations with the Flame Speed Closure (FSC) model implemented in the OpenFOAM® environment are performed to obtain the flame describing function of the combustor set-up. The standard FSC model is extended in this work to take into account the combined effect of strain and heat losses on the flame. As a second step, a linear three-time-lag-distributed model for a perfectly premixed swirl-stabilized flame is extended to the nonlinear regime. The factors causing changes in the model parameters when applying high-amplitude velocity perturbations are analysed. As a third step, time-domain simulations employing a low-order network model implemented in Simulink® are performed. In this work, the proposed method is applied to a laboratory test rig. The proposed method permits not only the unsteady frequencies of acoustic oscillations to be computed, but the amplitudes of such oscillations as well. Knowing the amplitudes of unstable pressure oscillations, it is possible to determine how these oscillations are harmful to the combustor equipment. The proposed method has a low cost because it does not require any license for computational fluid dynamics software.

Keywords: combustion instabilities; limit cycle; time-domain simulations; URANS; FSC model

1. Introduction

Nowadays gas turbine manufacturers have to meet ecological requirements, particularly emissions of NO_x. These requirements force gas turbines that operate in the lean combustion regime to be produced. However, operation in the lean combustion regime is characterized by the high probability of occurrence of combustion instabilities (see [1–3]), which may cause catastrophic damage. This requires prevention of combustion instabilities which, in turn, requires understanding the nature of their onset.

There are different methods and numerical tools for the prediction of combustion instabilities. Since the thermo-acoustic phenomena in gas turbines include unsteady turbulent combustion, it is naturally to start with the analysis of these methods from Computational Fluid Dynamics (CFD). There are different approaches to performing complete

*Corresponding author. Email: dmytro.iurashev@edu.unige.it

CFD simulations of the unsteady flame–acoustic interaction of combustion systems: Unsteady Reynolds-Averaged Navier–Stokes (URANS) simulations; Large Eddy Simulations (LESs); and Direct Numerical Simulations (DNSs) [4]. These methods differ in their range of turbulent scales that are modelled versus those that are resolved. DNS resolves the entire range of turbulent length scales, thus this method gives the highest possible precision. Using the LES technique, the smallest scales of the turbulent flow are modelled while the largest and most important scales are resolved. In the URANS approach, all the turbulent scales are modelled, which makes it computationally the least expensive approach. The price of DNS precision is the computational cost, which depends cubically on the Reynolds number of the flow under consideration. Because of its high cost, DNS methods up to now have been applied only to simulate the closed-loop combustion–acoustic interaction of laminar flames with a very small computational domain [5,6]. LES was recently used to analyse the onset of thermo-acoustic instabilities in a laboratory-scale combustor [7], a self-excited azimuthal mode in a helicopter combustion chamber [8], and transverse and radial modes in a liquid rocket engine [9].

Some researchers perform low-Mach number or 'incompressible' LES to compute forced flame response [10,11]. In this case, the simulation time step can be increased since the speed of sound does not appear in the Courant–Friedrichs–Lewy (CFL) time-step limit, which results in faster CFD simulations. However, the results of such simulations can be different from those of compressible LES [12]. Compressible LES methods give very good precision, and continuous improvement of the computational capabilities of high-performance computing clusters will make its use more common. Nevertheless, nowadays they still remain computationally expensive. This is the reason for the use of URANS CFD calculations in this work.

Nonlinear CFD simulations of thermo-acoustic processes in the whole of gas turbine chambers with complex geometries in the time domain are computationally expensive. Since the thermo-acoustic problem is a multiscale phenomenon, in most thermo-acoustic studies combined approaches are employed. This means that the analysis of turbulent reacting flow is conducted apart from the acoustic analysis, and it is done for the sake of reducing the computational time. Acoustic length- and time-scales are often considered to be much larger than chemical and turbulent scales. This makes it possible to perform simulations of turbulent combustion and acoustics separately, using different tools. This decoupling is artificial but it helps to simplify the analysis. The heat response to acoustic and stoichiometry perturbations is usually computed experimentally [13–15] or numerically [16,17] performing unsteady analysis and is the input for the network model. Because of the high costs, difficulties, and uncertainties of the experimental heat response computation [18], CFD methods are now widely used. For acoustic analysis, either network models, Computational Acoustics (CA) or Computational Aero-Acoustics (CAA) methods are employed.

The analysis of linear waves is made easier when the cross-sectional dimension of the combustor is small compared with the acoustic wavelength [19]. Then, acoustic modes with variations across the cross section are 'cut-off', decaying with the axial position rather than propagating, and variations of the acoustic waves across the cross section can be neglected. This leads to plane waves in a cylindrical combustor, and axial and circumferential waves in an annular combustor. The frequencies of interest for combustion instabilities in gas turbines are sufficiently low that this is often a good approximation. Then, the linear wave equations can be solved semi-analytically by a network approach [20–23]. This enables physical insight into important mechanisms. The set-up is divided into a set of ducts with constant cross section and constant thermophysical properties. Acoustic waves propagate along the ducts and are connected between neighbouring ducts through transfer matrices

[24]. The Green's function approach introduced by Heckl [25] is similar to the network model approach. The flame is modelled in the network model as one or as a number of compact heat sources [26].

The following groups of analyses are CA and CAA methods. Both of these approaches are applicable to complex three-dimensional geometries of gas turbine combustion systems. The CA approach solves the inhomogeneous Helmholtz equation using, for example, the Finite Element Method (FEM) (see Camporeale *et al.* [27]). In this approach, mean flow and viscous effects on the acoustic field are neglected. In the CAA approach, either the Linearized Euler Equations (LEEs) [28,29] or the Linearized Navier–Stokes Equations (LNSEs) are resolved [29]. Both the LEE and the LNSE approaches take into account the mean flow. The difference between the two approaches is that LEE neglects viscous effects, while LNSE takes them into consideration. Despite its simplifications, various Helmholtz solvers are widely used in the industrial setting to forecast combustion instabilities.

Numerical tools for thermo-acoustic analysis can be divided into two large groups: frequency domain analyses [27,30] and time domain simulations [31,32]. The first type of analysis is usually used in the linear setting, i.e. to predict whether the set-up is stable or not [27]. It can also be used to predict the amplitude of unstable pressure fluctuations. To accomplish this task, Silva *et al.* [33] proposed performing simulations for each amplitude of acoustic oscillation that is characterized by its own Flame Transfer Function (FTF). The value of acoustic oscillation amplitude that corresponds to zero growth rate is considered as the amplitude of saturated oscillations. The procedure requires performing a set of several simulations with different FTFs. On the contrary, using time-domain analysis, unstable frequencies and their amplitudes are computed straightforwardly.

First, we model combustion dynamics with the help of Unsteady Reynolds-Averaged Navier–Stokes (URANS) simulations using the Flame Speed Closure (FSC) model proposed by [34] implemented in the OpenFOAM® environment [35]. The advantage of OpenFOAM® is that it is open-source software and does not require a license for its utilization. URANS simulations are suitable to predict flame-flow interaction in the low-frequency limit (see [36]). The FSC model does not resolve combustion chemistry but makes use of the regress variable approach. The chemistry is lumped with the laminar flame speed. This results in relatively fast computations. Moreover, the FSC model used in the present work is extended to take into account the combined quenching effect of strain and heat losses on the flame [37].

Researchers and engineers often perform linear stability analyses. This type of analysis allows the stable and unstable frequencies of thermo-acoustic systems to be predicted and makes use of FTFs – the response of the flame to small-amplitude velocity perturbations [38–40]. To forecast not only the frequency of pressure oscillations but also their amplitude, the Flame Describing Function (FDF) – the response of the flame to velocity perturbations at different amplitudes – should be known both for analyses in the frequency domain [14] and in the time domain [32]. This type of analysis is called weakly nonlinear since the acoustics are still assumed to be linear but the heat release response is dependent on the amplitude of velocity excitation.

In this work, we discuss the Beschaufelter RingSpalt (BRS) test rig developed by Komarek and Polifke [13] at the Technische Universität München. The authors of [13] investigated the response of the flame to axial and tangential components of velocity excitations for a perfectly premixed swirl-stabilized flame and proposed an analytical model for the flame response to small-amplitude velocity excitations. However, this model is limited to the linear regime of excitation. In this paper we extend the linear analysis of Komarek and Polifke [13], performing simulations with different amplitudes of velocity

excitation at several frequencies, obtaining the FDF. The obtained FDF is then approximated with a new analytical model.

Finally, we use a simplified wave-based approach implemented in Simulink® to find stability margins of parameters under which gas turbines could be operated without going into self-excited pressure oscillations. Li and Morgans [32] have shown that thermo-acoustic simulations in the time domain using the wave-based approach with a nonlinear flame model could predict different nonlinear behaviours of the system. The usage of an ad hoc network model gives freedom in model settings.

The paper is structured as follows. First, the theoretical background of the first and the third step is explained. In the second section, the FDF of the BRS set-up is presented, calculated performing URANS simulations with the FSC model implemented in an OpenFOAM® environment. In the third section, an analytical model for the FDF is introduced and the meaning of the parameters' dependence on the amplitude of acoustic perturbations is explained. A stability analysis of the BRS test rig is performed using time-domain network model simulations in the fourth section, where both linear and nonlinear parametric analyses are done. The findings of the work are summed up in the last section.

2. Background

2.1. *Description of the flame speed closure model*

In order to model combustion in the BRS test rig, we use the FSC model (see [34]). Compared to the Turbulence Flame Speed (TFC) model developed by Karpov *et al.* [41], the FSC model describes the propagation of the flame not only in the case of fully developed turbulence but also in the limit case of the absence of turbulence. Moreover, it takes into account the dependence of turbulent diffusivity and turbulent flame speed on the time of flow propagation from the flame holder to the flame front. We have implemented the FSC model into the *XiFoam* solver of OpenFOAM® [42]. This is a solver for the simulation of compressible premixed/partially-premixed combustion with turbulence modelling. It uses the compressible PIMPLE (merged PISO-SIMPLE) algorithm. The solver makes use of the regress variable, i.e. the normalized fuel mass fraction, defined as

$$b = \frac{T_b - T}{T_b - T_u}, \tag{1}$$

where T_b is the temperature of the burnt gas, T is the gas temperature at the current point, and T_u is the temperature of the unburnt gas. Thus, the regress variable is equal to one in the unburnt gas zone and zero in the burnt gas zone. The transport equation for the regress variable is

$$\frac{\partial \rho b}{\partial t} + \nabla \cdot (\rho \boldsymbol{u} b) - \nabla \cdot \left[\rho(\kappa + D_{t,t})\nabla b\right] = -\frac{S_{L,0}^2}{4(\kappa + D_{t,t})}\rho_u(1-b)b - \rho_u S_{t,t}|\nabla b|, \tag{2}$$

where ρ is the density of the air–fuel mixture, t is the time, $\boldsymbol{u}$ is the velocity vector, κ is the molecular diffusivity, $D_{t,\,t}$ is the time-dependent coefficient of turbulent diffusion, $S_{L,\,0}$ is the unperturbed laminar flame speed, and $S_{t,\,t}$ is the time-dependent turbulent flame velocity. Definitions of these parameters can be found in the work of Lipatnikov and Chomiak [34].

The standard FSC model is extended in this work in order to take into account the combined influence of the strain and heat losses on the flame [37]. The turbulent flame

speed S_t is calculated as

$$S_t = 0.52(u'_{\text{turb}})^{0.75} S_{\text{cons}}^{0.5} \alpha_u^{-0.25} l_t^{0.25}, \tag{3}$$

where u'_{turb} is the turbulent velocity perturbation, S_{cons} is the consumption speed of a laminar premixed flame, α_u is the thermal diffusivity of the unburnt mixture, and l_t is the turbulence length scale. The consumption speed is calculated as suggested by Tay-Wo-Chong *et al.* [37].

The right-hand-side of Equation (2) is the mass flow rate of the mixture passing through the set-up. Thus, the heat release rate is calculated as

$$\dot{Q} = Y_f H_R \left[\frac{S_{L,0}^2}{4(\kappa + D_{t,t})} \rho_u (1-b) b + \rho_u S_{t,t} |\nabla b| \right], \tag{4}$$

where Y_f is the fuel mass ratio and H_R is the lower heating value of the fuel.

2.2. *The flame transfer function*

The dynamic response of a flame to a flow perturbation of small amplitude can be represented in the frequency domain by its $FTF(\omega)$ (also called the frequency response of the flame). It relates fluctuations of mass flow rate or velocity $\hat{u}_r$ at a reference position r upstream of the flame to fluctuations of the flame heat release $\hat{\dot{Q}}$ for a range of angular frequencies ω

$$FTF(\omega) = \frac{\hat{\dot{Q}}(\omega)/\bar{\dot{Q}}}{\hat{u}_r(\omega)/\bar{u}_r}. \tag{5}$$

Here, fluctuations $\hat{\dot{Q}}$ and $\hat{u}_r$ are normalized against the respective mean values of heat release $\bar{\dot{Q}}$ and velocity $\bar{u}_r$. In experiments, the flame transfer function $FTF(\omega)$ is computed from time series of fluctuations $u'_r(t)$ and $\dot{Q}'(t)$ with spectral analysis applying harmonic excitation with a loudspeaker or siren at the inlet.

The FTF from the numerical simulations is calculated using the Wiener–Hopf Inversion (WHI). Application of the WHI to results of unsteady CFD simulations was initially proposed by Polifke *et al.* [43]. This method permits the FTF to be computed in a wide range of frequencies by performing just one simulation. Thus, the time for the FTF calculations is reduced significantly.

2.3. *The flame describing function*

In general, the response of the flame to velocity perturbations depends not only on the frequency of the perturbation but also on its amplitude. Thus, if one would like to perform amplitude-dependent stability analysis of a thermo-acoustic system, the FDF should be known:

$$FDF(\omega, A) = \frac{\hat{\dot{Q}}(\omega, A)/\bar{\dot{Q}}}{\hat{u}_r(\omega, A)/\bar{u}_r}, \tag{6}$$

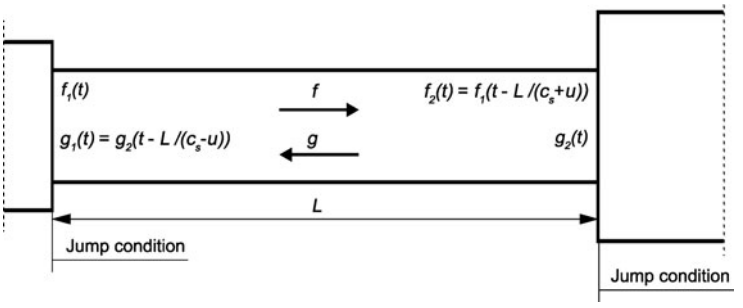

Figure 1. Scheme of waves propagation in a section of a low-order model.

where A is the normalized amplitude of velocity perturbations at the reference point.

Unfortunately, advanced methods such as WHI can be used only in linear cases, i.e. the response of the flame to small amplitudes of velocity perturbations. Thus, in order to compute the FDF, we have to apply only one frequency excitation with one amplitude per simulation.

2.4. *Wave-based approach for thermo-acoustic simulations*

When the length of the set-up under consideration is much larger than its dimensions in the other directions, it is possible to perform a one-dimensional low-order acoustic analysis.

The test rig is divided into a set of sections with constant cross-sectional area. Pressure, velocity, temperature, and density are decomposed into the sum of their mean components (denoted by ‘ $\bar{}$ ’) and their fluctuating component (denoted by ‘ $'$ ’). Mean values of pressure, velocity, temperature, density and thermophysical properties are assumed to be constant along each section and change only from section to section.

Perturbations of pressure and velocity could be represented in terms of downstream and upstream propagating acoustic waves (characteristics) (see Figure 1):

$$p'(x,t) = f\left(t - \frac{x}{\bar{c}_s + \bar{u}}\right) + g\left(t + \frac{x}{\bar{c}_s - \bar{u}}\right), \tag{7}$$

$$u'(x,t) = \frac{1}{\bar{\rho}\bar{c}_s}\left[f\left(t - \frac{x}{\bar{c}_s + \bar{u}}\right) - g\left(t + \frac{x}{\bar{c}_s - \bar{u}}\right)\right], \tag{8}$$

where p is the pressure, f and g are downstream and upstream travelling components (Riemann invariants) of acoustic waves, respectively, $\bar{c}_s$ is the mean speed of sound, u is the velocity, and ρ is the density. The entropy waves are neglected in the network model since the set-up is perfectly premixed and it is assumed that no entropy perturbation enters the set-up.

In order to connect oscillating variables in different sections (see Figure 2) we need to know the so-called jump conditions. To compute the jump conditions between sections separated by a compact acoustic element, such as a sharp cross-sectional area change and a compact swirler, the system of linearized equations – conservation of mass equation and Bernoulli equation – has to be written in terms of f and g as suggested by Dowling and Stow [44]. We can write the system of equations in the case of area change in matrix form

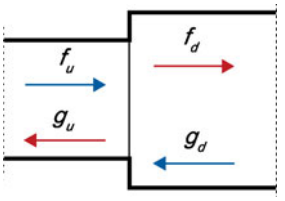

Figure 2. Scheme of waves propagation between sections of a low-order model. (Colour online)

as follows:

$$\mathbf{F}\begin{bmatrix} f_d \\ g_u \end{bmatrix} = \mathbf{K}\begin{bmatrix} f_u \\ g_d \end{bmatrix}, \tag{9}$$

where subscripts u and d denote upstream and downstream sections, respectively. Matrices **F** and **K** take into account acoustic losses between sections; their coefficients can be found in Appendix A.

To calculate jump conditions at the flame, the system of linearized equations of conservation of momentum and energy (product of mass conservation equation and Bernoulli equation) has to be written in terms of f and g [44]. The system of equations in matrix form at the flame is

$$\mathbf{J}\begin{bmatrix} f_d \\ g_u \end{bmatrix} = \mathbf{H}\begin{bmatrix} f_u \\ g_d \\ \dot{Q}' \end{bmatrix}, \tag{10}$$

where the coefficients of matrices **J** and **H** can be found in Appendix A.

At the beginning of the first section and at the end of the last section, the f and g waves are related by the reflection coefficients R_{inlet} and R_{outlet}, respectively.

3. Step 1. Modelling the flame describing function

3.1. *Description of the experimental set-up*

The test rig under consideration is operated under atmospheric pressure and consists of three main parts: a plenum, a swirl stabilized burner with a central bluff body, and a combustion chamber (see Figure 3). The perfectly premixed mixture of methane and air with equivalence ratio equal to 0.77 enters in the set-up. A rigid sinter plate is placed at the beginning of the plenum. The burner exit is represented by an annular section with an inner diameter of 16 mm and an outer diameter of 40 mm. The swirler consists of eight blades, has length 30 mm, and is positioned 30 mm upstream of the burner exit. The combustion chamber has a quadratic cross section of 90×90 mm^2. The length of the combustion chamber is variable and during FTF measurements was kept equal to 300 mm. A perforated plate is placed at the end of the combustion chamber in order to ensure a low reflective acoustic boundary condition. In the experiments, the position of the heat release distribution was determined by OH* chemiluminescence measurements. The walls of the experimental set-up under consideration are water cooled so that strong heat losses occur [45]. In our investigation, the thermal power is equal to 30 kW. Further details about the experimental set-up can be found in the work of Komarek and Polifke [13].

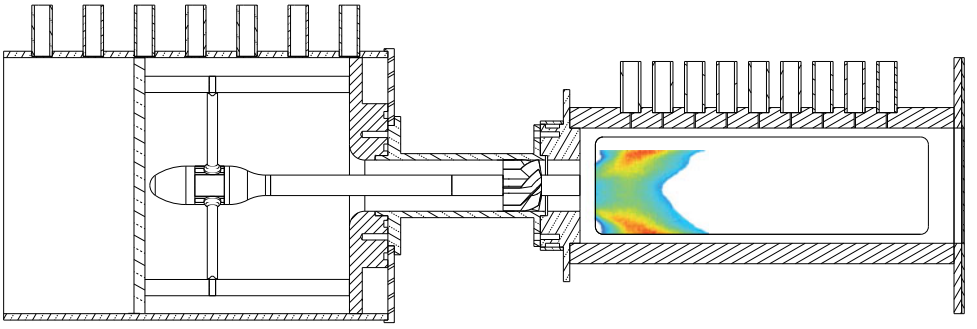

Figure 3. Scheme of the BRS test rig © [Thomas Komarek]. Reproduced by permission of Thomas Komarek. (Colour online)

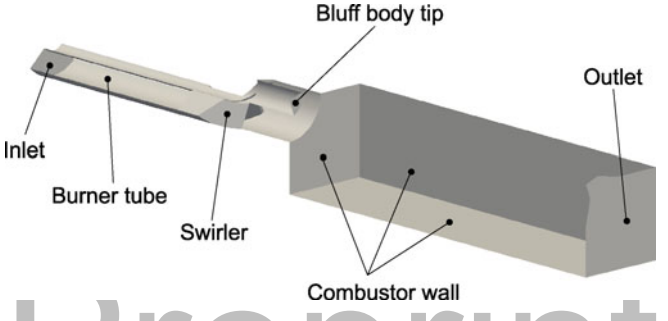

Figure 4. Sector scheme of the numerical set-up of the BRS test rig.

3.2. *Description of the numerical set-up*

A 3D structured mesh consisting of around 280,000 cells was created using the commercial software ANSYS® ICEM CFD™. Since the structure of the set-up is periodic, just one quarter of the test rig has been modelled in the simulations (see Figure 4). The heat release zone lies within the first 100 mm of the combustion chamber and the recirculation zones lie within 200 mm from the entrance of the combustion chamber, as reported by Komarek and Polifke [13]. Thus, the combustor length of 200 mm is enough to simulate the behaviour of the flame. The time step of the simulations is 4×10^{-7} s to ensure an acoustic CFL number lower than 0.7. The Launder–Reece–Rodi Reynolds-stress turbulence model [46] is used, which is required for the correct calculation of the consumption speed [37]. The automatic wall functions used provide a turbulent dynamic viscosity (μ_t) condition for rough walls, based on velocity, using Spalding's law to give a continuous μ_t profile to the wall [42].

To avoid the development of resonance modes, non-reflective or partially reflective boundary conditions at both inlet and outlet have been employed. We make use of the *waveTransmissive* boundary condition implemented in OpenFOAM® [42], which is based on the work of Poinsot and Lele [47], and is expressed by the following equation for the pressure at the boundaries:

$$\frac{\partial p}{\partial t} + u_{\text{wave}} \frac{\partial p}{\partial x} = \frac{u_{\text{wave}}}{l_{\text{inf}}} (p_{\text{inf}} - p), \tag{11}$$

where $u_{\text{wave}} = u + c_s$ at the outlet, $u_{\text{wave}} = u - c_s$ at the inlet, c_s is the speed of sound, and l_{inf} is the distance from the boundary (outlet or inlet) at which the pressure field p becomes

Table 1. Boundary conditions for the BRS numerical model.

Face	Boundary condition	Details
Inlet	Velocity inlet	11.3 m/s
Outlet	Pressure outlet	101,325 Pa
Burner tube, swirler	Adiabatic no-slip wall	–
Combustor wall	Isothermal no-slip wall	600 K
Bluff body tip	Isothermal no-slip wall	600 K

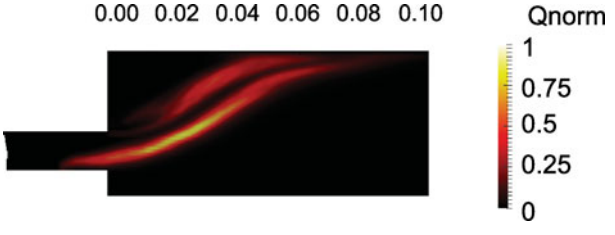

Figure 5. Normalized unperturbed heat release distribution from simulation averaged over 35 m/s. (Colour online)

equal to p_{inf}. In this work, $l_{\text{inf}} = 1$ m, which guarantees both low reflection coefficients and numerical stability. Boundary conditions for the unperturbed simulation are listed in Table 1. The walls of the combustion chamber and of the burner tip are imposed as isothermal in order to take into account the heat losses [16].

3.3. *Results of unperturbed simulations*

In a previous work of ours [35], a sensitivity analysis of the parameters of the FSC model was described. As a result, the following values of parameters were chosen: the turbulent Schmidt number $\text{Sc}_t = 0.3$, the model constant $C_D = 0.3$, and the axial flow velocity at the burner exit $u_{\text{FSC}} = 18$ m/s.

The surface distribution of the heat release averaged over 35 m/s of simulations is shown in Figure 5. The quenching effect of heat losses and strain is clearly seen in the outer shear layer of the flame (see Figure 5).

It is illustrative to compare the heat release distributions in experiments and simulations along the longitudinal axis. To obtain this distribution from our simulation we take several planes perpendicular to the longitudinal axis in the range −0.02–0.12 m from the entrance of the combustion chamber in the axial direction. Then, we integrate the heat release over these planes and plot the resulting values over the longitudinal axis (see Figure 6). The experimental heat release distribution is normalized by its maximum value. The numerical heat release distribution is normalized such that the integrals from the two distributions are the same in the range known from experiments [16].

3.4. *Numerical calculation of the flame transfer function*

A transient numerical simulation of the system is performed by exciting the axial component of velocity at the inlet of the computational domain. The excitation signal is composed of a sum of sine waves with random frequencies in the range 0–1 kHz and of random phase. The excitation signal is normalized such that three standard deviations of the signal amplitude

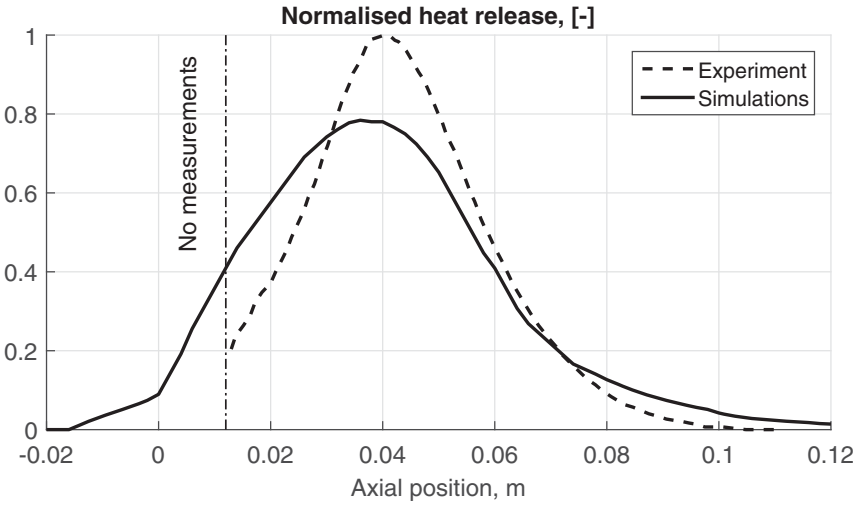

Figure 6. OH* chemiluminescence distribution from experiment and heat release distribution from the simulation.

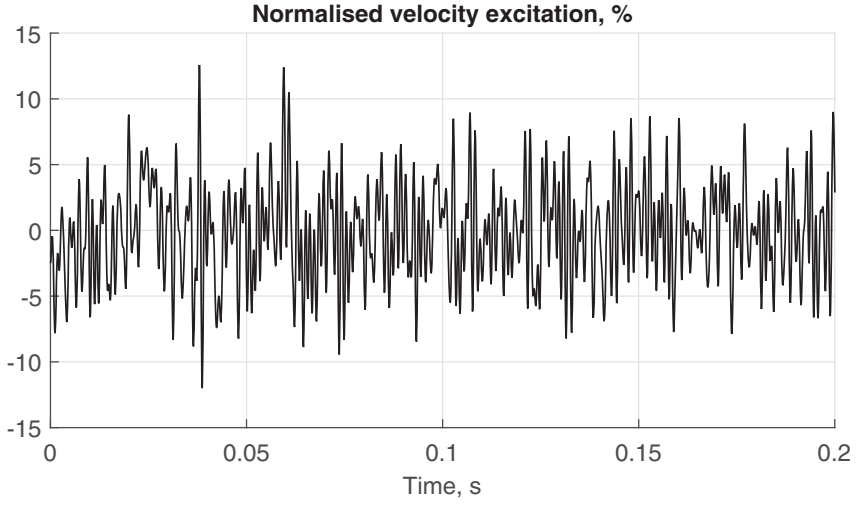

Figure 7. Velocity excitation used in the FTF calculation.

are equal to 10% of the mean velocity at the inlet of the computational domain; this is shown in Figure 7. The fast Fourier transform of the velocity excitation signal is shown in Figure 8.

The time series u_r is composed during the simulations as the axial component of velocity averaged in a plane perpendicular to the z-axis situated 2 cm upstream of the burner exit (1 cm downstream of the swirler). The flame response $\dot{Q}$ is measured in simulations as the volumetric integral of Equation (4). After that, the mean values $\bar{u}_r$ and $\bar{\dot{Q}}$ of the measured u_r and $\dot{Q}$ are computed and are subtracted from series of u_r and $\dot{Q}$, respectively, in order to obtain fluctuations of the axial velocity u'_r and fluctuations of the heat release $\dot{Q}'$.

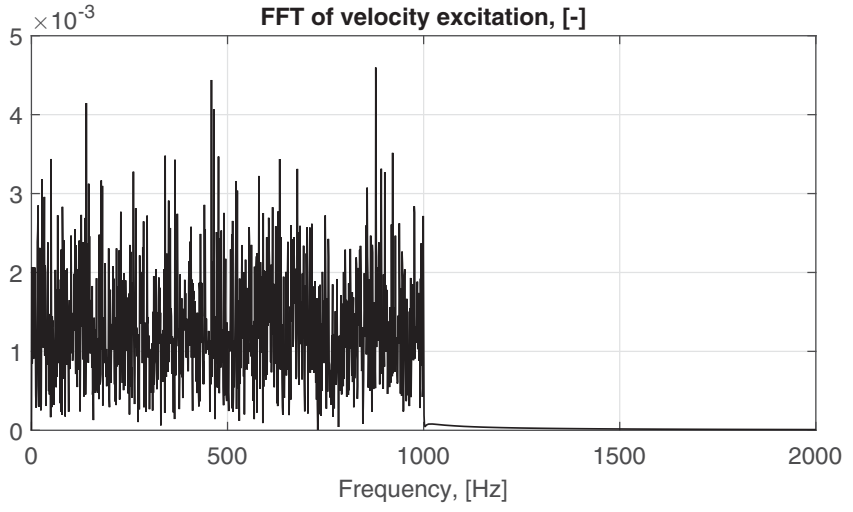

Figure 8. The Fast Fourier Transform (FFT) of the velocity excitation used in the FTF calculation.

The simulation is run for 200 m/s in real time. Longer simulation times do not change the FTF. The duration of the Unit Impulse Response (UIR) is assumed to be equal to 12 m/s. The first 15 m/s are considered as a transition period and are neglected. Using the Wiener–Hopf inversion method described before, the FTF of the BRS test rig is calculated and is shown in Figure 9.

There is good agreement between the experimentally obtained FTF and that computed from simulations in terms of the phase in the range of frequencies 0–200 Hz. The underestimated gain of the FTF is explained by the more dispersed heat release distribution from simulations with respect to the experimental one as shown in Figure 6.

3.5. *Numerically computed flame describing function*

In order to construct the FDF, excitation frequencies of 100, 160, 240, and 320 Hz are chosen; 160, 240, and 320 Hz are equidistantly distributed; 100 Hz is chosen instead of 80 Hz since instability was observed in the experiment at 101.3 Hz [16]. Different excitation amplitudes of velocity perturbations are applied at the inlet of the numerical set-up in order to obtain velocity perturbations after the swirler with amplitudes of 30, 50, and 70% for each frequency.

The FDF obtained from the simulations is shown in Figure 10. The most significant decay of the gain of the FDF with increasing amplitude of the velocity perturbations is observed at 100 Hz (see Figure 10). The most significant change in phase of the FDF is observed at 240 Hz (see Figure 10).

The reason for the variation of the phase of the FDF for different amplitudes of excitation can be explained as follows. When high-amplitude velocity excitations are applied, the turbulence of the flow in the combustor is intensified. This results in higher turbulent flame velocity and, as a result, the shift of the heat release distribution towards the entrance of the combustion chamber (see Figures 11 and 12). The results of the simulations with high-amplitude excitation at 240 Hz are shown in this paper, but similar behaviours are observed with excitations at other frequencies. Similar flame behaviour was also observed during

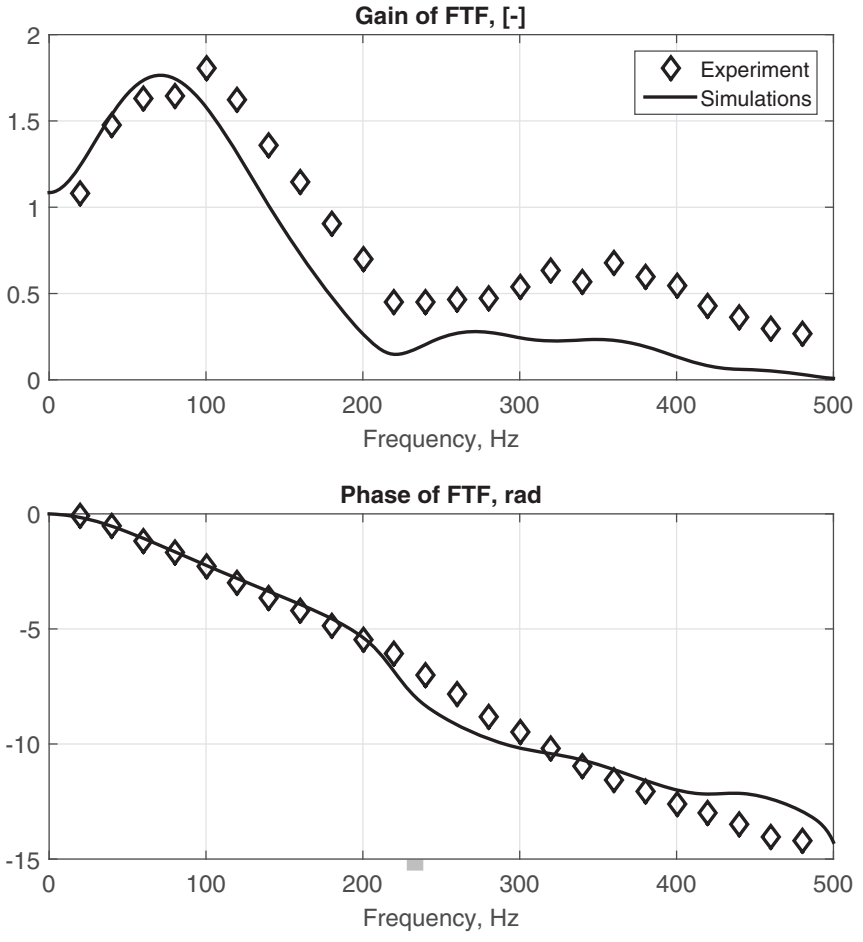

Figure 9. FTF calculated experimentally and from simulations.

LES of limit-cycle oscillations in a rocket engine [9]. Note that the flame length, i.e. the length of non-zero heat release averaged over one cycle of perturbation, remains the same as in the unperturbed simulation. Further insight on the change of the FTF phase is given in Section 4.1.

4. Step 2. Analytical FDF models

4.1. *URANS FDF model*

Komarek and Polifke [13] have proposed the following model for the FTF in the case of perfectly premixed swirl-stabilized combustion:

$$FTF(\omega) = \mathrm{e}^{-\mathrm{i}\omega\tau_1 - 0.5\omega^2\sigma_1^2} + a\left(\mathrm{e}^{-\mathrm{i}\omega\tau_2 - 0.5\omega^2\sigma_2^2} - \mathrm{e}^{-\mathrm{i}\omega\tau_3 - 0.5\omega^2\sigma_3^2}\right), \tag{12}$$

where τ_i is the time delay of the corresponding mechanism, σ_i is the standard deviation of the corresponding time delay, and a is a dimensionless constant. The response of the

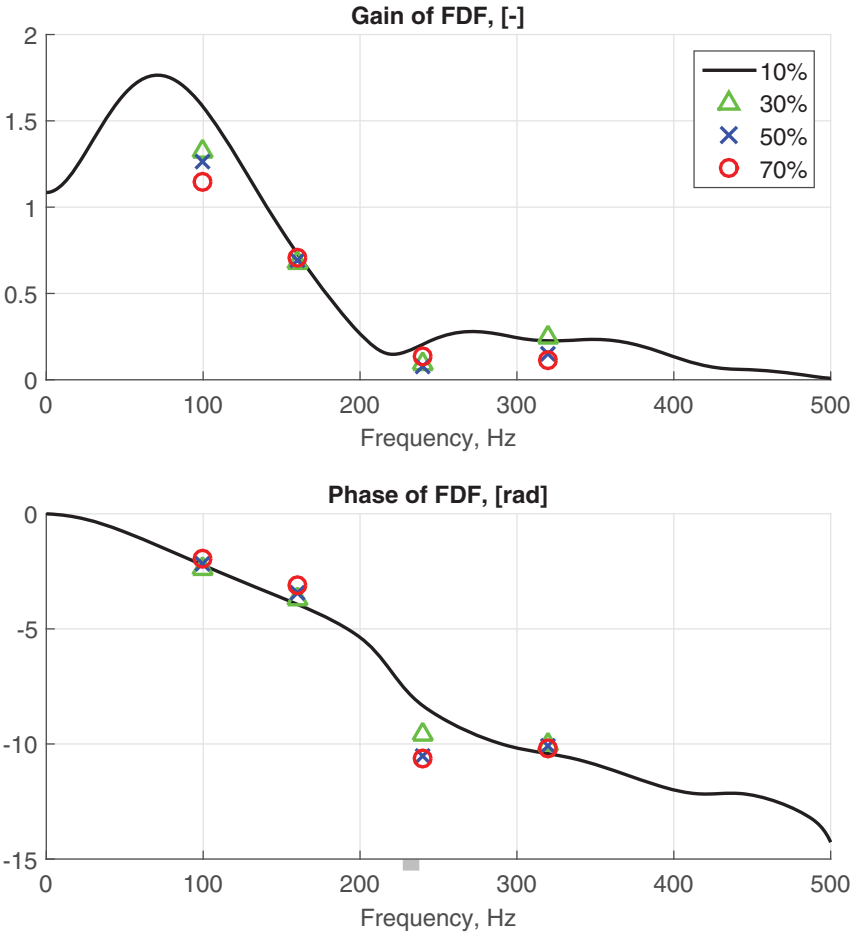

Figure 10. FTF (continuous line) and FDF (points) computed from simulations. (Colour online)

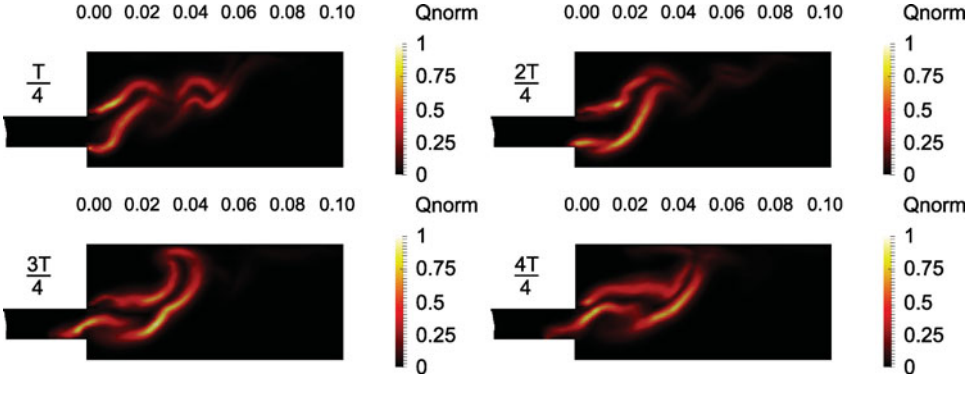

Figure 11. Heat release distribution in the set-up at different instants of a period of oscillation (excitation at 240 Hz with amplitude 70%). (Colour online)

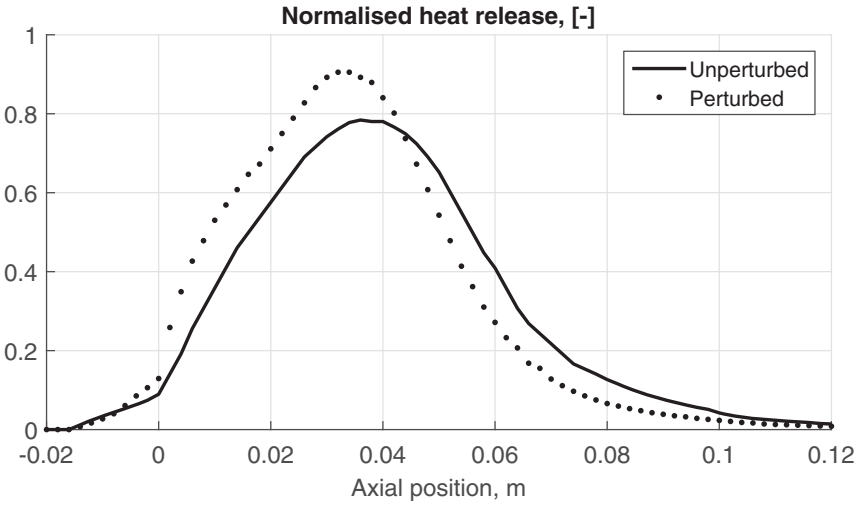

Figure 12. Averaged heat release distribution in the set-up without perturbation and heat release distribution averaged over one period of oscillation (excitation at 240 Hz with amplitude 70%).

flame to the axial perturbations of the velocity is modelled with the parameters τ_1 and σ_1. The parameters τ_2, σ_2, τ_3, and σ_3 model the response of the heat release to the tangential perturbations of the velocity produced by a swirler. With respect to the original model [13], Tay-Wo-Chong *et al.* [45] introduced the dimensionless parameter $a = 1.05$ in Equation (12), which gives better agreement with the measured FTF.

In this paper, the model given in Equation (12) is extended to the nonlinear regime by introducing the dependence of the parameters τ_i and σ_i on the amplitude of velocity excitation:

$$FDF(\omega, A) = \mathrm{e}^{-\mathrm{i}\omega\tau_1(A)-0.5[\omega\sigma_1(A)]^2} + a\left\{\mathrm{e}^{-\mathrm{i}\omega\tau_2(A)-0.5[\omega\sigma_2(A)]^2} - \mathrm{e}^{-\mathrm{i}\omega\tau_3(A)-0.5[\omega\sigma_3(A)]^2}\right\}. \tag{13}$$

First, we calculate the optimum values of τ_i and σ_i for each amplitude of velocity perturbation using the method of least squares. The obtained values of parameters τ_i and σ_i for different amplitudes of perturbation are presented in Table 2 and the corresponding modelled FDF is shown in Figure 13. All τ_i decrease with increasing A. This trend is explained by the heat release distribution peak shift towards the swirler when the flame is forced with high-amplitude excitation. The increase of σ_2 and σ_3 while increasing A

Table 2. Values of parameters τ_i and σ_i for different amplitudes of perturbation (ms).

Amplitude (%)	τ_1	σ_1	τ_2	σ_2	τ_3	σ_3
10	2.57	1.01	4.96	0.93	7.00	1.69
30	2.43	0.90	4.54	0.96	5.65	2.50
50	2.37	0.91	4.39	0.98	5.09	2.50
70	2.30	0.92	4.17	1.03	3.96	2.50

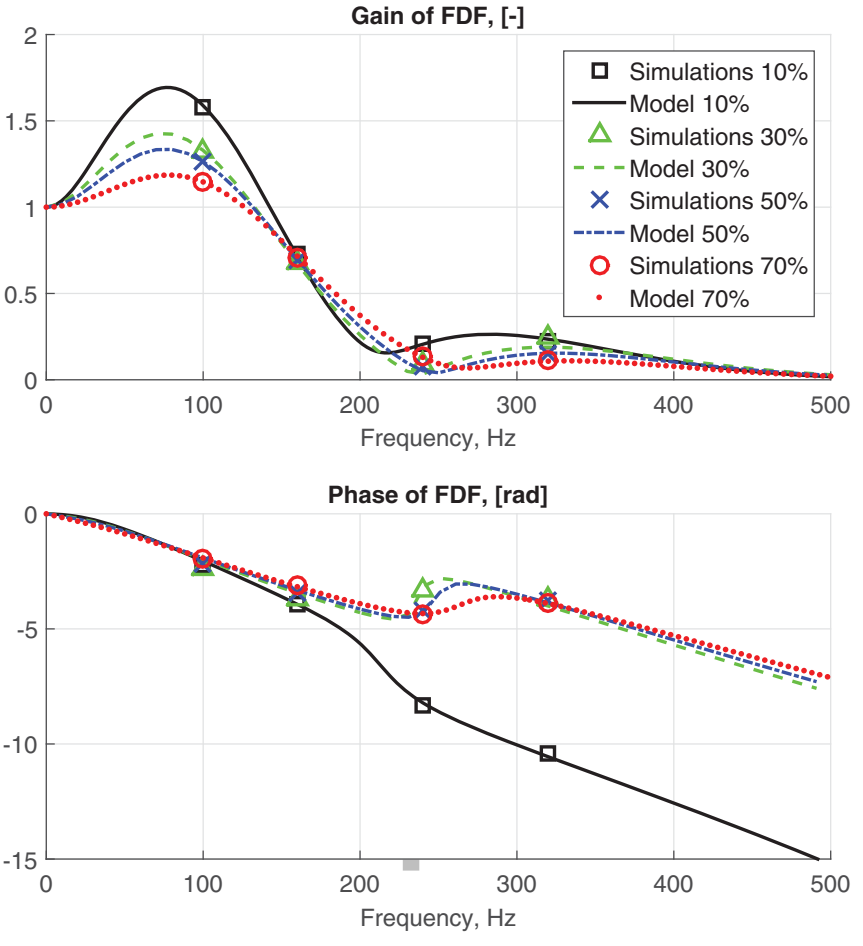

Figure 13. FDF computed from simulations and modelled with Equation (13). (Colour online)

is explained by higher dispersion of the flame when applying high-amplitude excitation (see Figure 12); σ_1 slightly decreases while increasing A, which could be influenced by the second time delay τ_2 and its standard deviation σ_2. The values of the FDF phase at 240 and 320 Hz for high-amplitude excitations are shifted by 2π with respect to the ones shown in Figure 10 in order to guarantee the continuous lines of the FDF model.

Secondly, the dependence of τ_i and σ_i on the normalized amplitude of velocity perturbations A are modelled as

$$\tau_i = \tau_{i,\mathrm{lin}}(1 + \Theta_i A), \tag{14}$$

$$\sigma_i = \sigma_{i,\mathrm{lin}}(1 + \Sigma_i A), \tag{15}$$

where $\tau_{i,\,\mathrm{lin}}$ and $\sigma_{i,\,\mathrm{lin}}$ are values of the parameters τ_i and σ_i for infinitesimal amplitude A, while Θ_i and Σ_i are dimensionless parameters that correspond to the relative change of the parameters τ_i and σ_i when $A = 1$. Linear dependencies $\tau_i(A)$ and $\sigma_i(A)$ are chosen because they give smaller values of root-mean-square errors than squared ones.

Table 3. Optimum values of parameters $\tau_{i,\,\mathrm{lin}}$, Θ_i, $\sigma_{i,\,\mathrm{lin}}$, and Σ_i.

i	$\tau_{i,\,\mathrm{lin}}$ (ms)	Θ_i (–)	$\sigma_{i,\,\mathrm{lin}}$ (ms)	Σ_i (–)
1	2.59	−0.168	0.99	−0.131
2	5.02	−0.251	0.91	0.176
3	7.36	−0.658	1.81	0.671

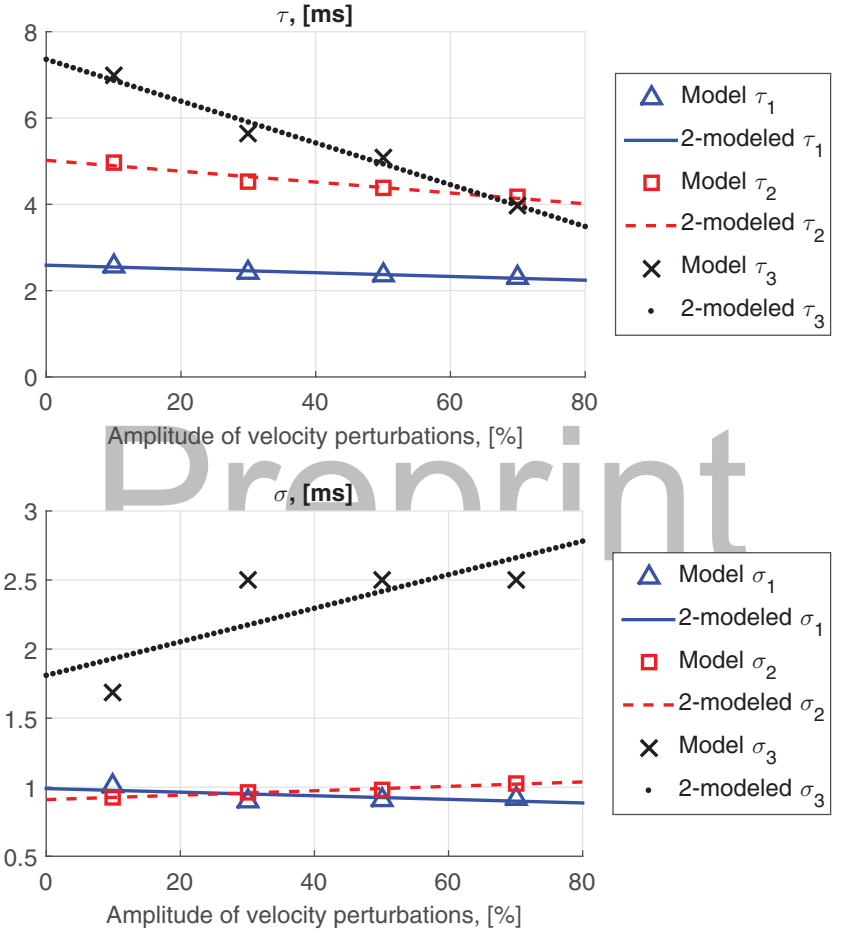

Figure 14. Dependencies $\tau_i(A)$ and $\sigma_i(A)$ from Table 2 (points, 'Model') and modelled by Equations (14) and (15) (lines, '2-modeled'). (Colour online)

Optimal values of parameters $\tau_{i,\,\mathrm{lin}}$, Θ_i, $\sigma_{i,\,\mathrm{lin}}$, and Σ_i are computed using the least squares method and are listed in Table 3. The resulting functions are shown in Figure 14 together with the values from Table 2. Equations (14) and (15) guarantee the continuity of the FDF model in Equation (13) for different excitation amplitudes.

The physical meaning of parameters τ_i and σ_i and of their dependence on A is understood if we switch from the frequency domain representation of the FTF to the time-domain representation, i.e. to the UIR. The UIR in this work is the response of the normalized heat

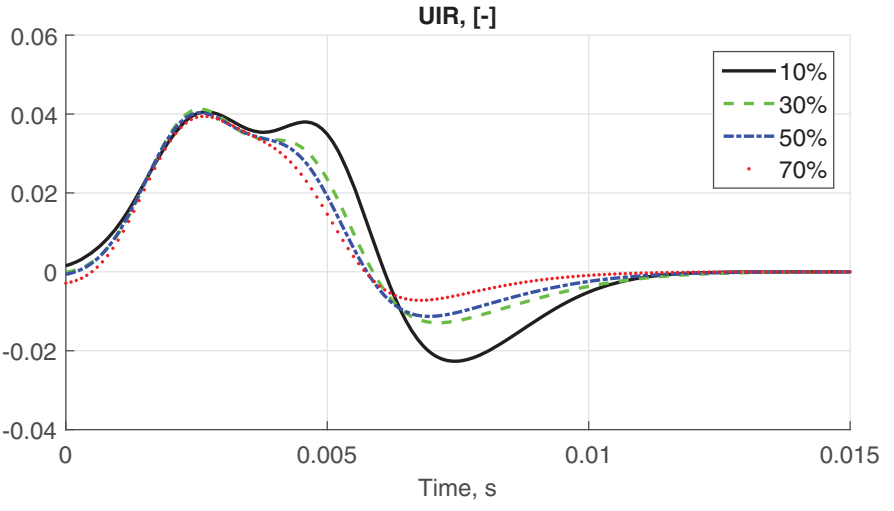

Figure 15. UIRs for different amplitudes of velocity excitations modelled by Equation (16). (Colour online)

release to the normalized velocity perturbation of unit amplitude. The analytical form of the UIR corresponding to the FTF of Equation (12) is

$$UIR(t) = \frac{1}{\sigma_1\sqrt{2\pi}} e^{-0.5[(t-\tau_1)/\sigma_1]^2} + a\left\{\frac{1}{\sigma_2\sqrt{2\pi}} e^{-0.5[(t-\tau_2)/\sigma_2]^2} - \frac{1}{\sigma_3\sqrt{2\pi}} e^{-0.5[(t-\tau_3)/\sigma_3]^2}\right\}. \tag{16}$$

Thus, Equation (16) models the response of the heat release to acoustic oscillations with the help of three Gaussians with peaks at τ_i and standard deviations σ_i. The UIRs for different amplitudes of velocity excitation are shown in Figure 15. As already mentioned in Section 3.5, high-amplitude velocity excitations intensify the turbulence of the flow and shift the peak of the heat release distribution towards the combustion chamber entrance (see Figure 12). This causes the flame response peaks in the UIR (see Figure 15) to occur earlier in time. Moreover, the length of the non-zero heat release distribution remains almost unchanged. That is why the overall response duration remains almost the same for the four amplitudes considered.

Note that the proposed FDF model consists of only six parameters. The FDF at a certain excitation amplitude computed for three frequencies gives six equations for the FDF model parameters estimation: three equations for the FDF gain and three equations for the FDF phase. From a mathematical point of view, it is possible to find optimum model parameters knowing the FDF just at three frequencies. With four frequencies, as used in the present work, the problem of the optimum parameters' search becomes even overestimated, improving the reliability of the obtained results. Thus, using the proposed FDF model it is possible to reduce the number of time-consuming CFD simulations for the FDF calculation, which is the advantage of this FDF model.

Table 4. Values of parameters τ_i and σ_i for the model of experimental FTF (ms).

τ_1	σ_1	τ_2	σ_2	τ_3	σ_3
2.79	0.88	4.88	0.52	6.76	1.48

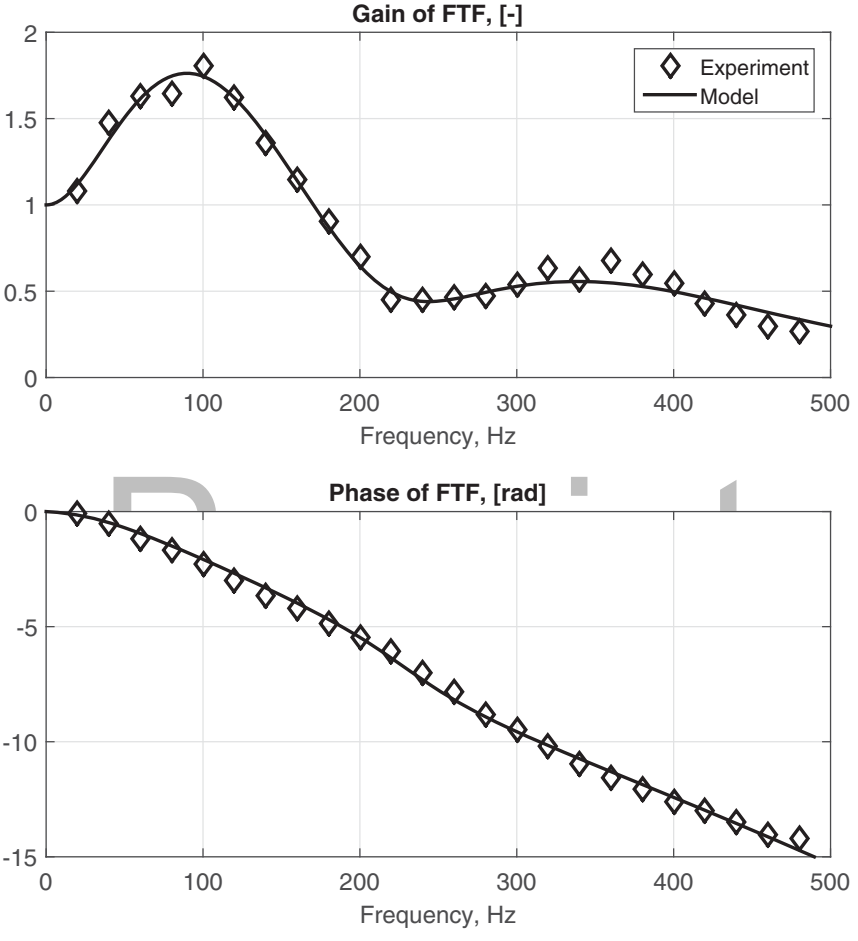

Figure 16. Experimental FTF and its model.

4.2. *Hybrid experimental–URANS FDF model*

It is possible to combine the FTF computed experimentally with the FDF computed with URANS simulations. First, the optimum values of τ_i and σ_i for the experimentally obtained FTF are calculated using the method of least squares and presented in Table 4. The corresponding model of the FTF is shown in Figure 16.

Then, the model described by Equations (13), (14), and (15) is assumed for the hybrid FDF. For infinitesimal perturbation amplitude, values of τ_i and σ_i correspond to the experimental FTF by taking the parameters $\tau_{i,\,\mathrm{lin}}$ and $\sigma_{i,\,\mathrm{lin}}$ from Table 4. Then, the change of parameters τ_i and σ_i with the amplitude is assumed to be the same as in the FDF model by

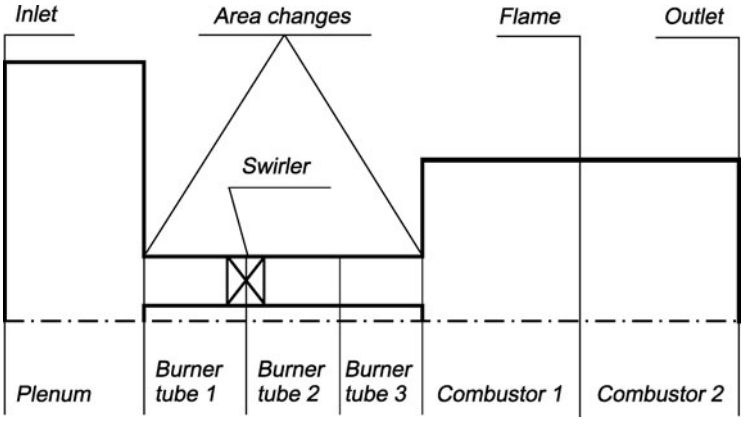

Figure 17. Scheme of numerical set-up divided into sections.

taking the dimensionless parameter values Θ_i and Σ_i from Table 3. As a result, the hybrid FDF model is constructed.

5. Step 3. Stability analysis using a wave-based approach

5.1. *Low-order network model set-up*

The numerical set-up has been divided into six regions with three jump conditions with pressure losses, one jump condition at the flame, and two boundary conditions as shown in Figure 17. The cross-sectional area, length, and temperature of each section are listed in Table 5. Jump matrices to connect waves between sections are calculated using systems of Equations (9) and (10). The reflection coefficient of the inlet is taken as $R_{\text{inlet}} = 1$. The outlet reflection coefficient $R_{\text{outlet}} = -0.35\text{e}^{-0.375^{-3}\text{i}\omega}$ is approximated from the values suggested by [16]. The total length of the combustor (sum of the lengths of *Combustor 1* and *Combustor 2*) $L_{\text{c.c.}}$ is varied in the range 0.3–0.95 m. Acoustic losses at area changes between plenum and burner tube and between burner tube and combustor are taken into account by coefficients of pressure losses $\zeta_{\text{decr}} = 0.487$ and $\zeta_{\text{incr}} = 0.756$, respectively [48]. Acoustic losses at the swirler are taken into account by the coefficient of pressure losses $\zeta_{\text{swirler}} = 2.073$ calculated from the unperturbed simulations. As noted by Tay-Wo-Chong and Polifke [45], the flame can be considered compact since its Helmholtz number is around 0.1 for the considered frequencies. The active flame, i.e. the unsteady heat release, in the low-order network model is positioned at $x_{\text{fl}} = 0.036$ m when the URANS FDF model is

Table 5. Values of parameters imposed in the network model.

N	Section	Area (m^2)	Length (m)	Temperature (K)
1	Plenum	$3.146E-2$	0.17	300
2	Burner tube 1	$1.056E-3$	0.135	300
3	Burner tube 2	$1.056E-3$	0.025	300
4	Burner tube 3	$1.056E-3$	0.02	300
5	Combustor 1	$8.1E-3$	x_{fl}	300
6	Combustor 2	$8.1E-3$	$L_{\text{c.c.}} - x_{\text{fl}}$	1930

used and at $x_{\mathrm{fl}} = 0.040$ m [16] when the hybrid FDF model is used. This values corresponds to the peaks of the heat release distributions in the longitudinal direction in the simulations and in the experiment, respectively (see Figure 6).

The mean temperature is uniform in the first five sections from *Plenum* till *Combustor 1* and is equal to 300 K. The speed of sound in these sections is 354 m/s and the heat capacity ratio is 1.399. The temperature gradient coincides with the position of the active flame and is situated between the sections *Combustor 1* and *Combustor 2*. The value of the temperature in the section *Combustor 2*, $T_{\mathrm{Combustor\,2}} = 1930$ K is taken from the work of Tay-Wo-Chong *et al.* [16]. The speed of sound in that section is 854 m/s and the heat capacity ratio is 1.268. This value is close to the adiabatic temperature of the flame (1960 K), which is observed in the inner recirculation zone in the simulation. Considering the case with the value of the temperature in the section *Combustor 2*, 1930 K makes possible the comparison of our results with the results of Tay-Wo-Chong *et al.* [16]. Stability analysis with $T_{\mathrm{Combustor\,2}} = 1712$ K that takes into account heat losses gives very similar results and is not presented in this work.

The velocity fluctuations for the unsteady heat release model are taken between sections *Burner tube 2* and *Burner tube 3*, which corresponds to the velocity reference position in the simulations. The instantaneous unsteady heat release is calculated as the convolution of the history of velocity fluctuations and the UIR:

$$Q'(t) = \frac{\bar{Q}}{\bar{u}} \int_0^\infty UIR_u^{\mathrm{mod}}(t' - t) u_r'(t)\, \mathrm{d}t', \tag{17}$$

where t' is the integration variable.

The normalized amplitude of velocity perturbations A is needed for the calculation of the instantaneous values of parameters τ_i and σ_i. The calculation of A is a challenge when using the FDF in time-domain simulations because it is unknown before the simulation is run and is rather the output of the simulation. In this work, the instantaneous value of A is computed as the maximum value of the normalized amplitude of velocity oscillations $\max(|u_r'|)/\bar{u}_r$ in a window of time that precedes the current instant of the simulation. Each time step of the UIR to be used in Equation (17) is recalculated based on the current amplitude of velocity perturbations A. This approach is robust and computationally inexpensive. The time window is taken as 25 m/s, which allows the normalized amplitude of the velocity oscillations to be computed for frequencies higher than 20 Hz. Smaller lengths of the time window may be required if the dynamics of the thermo-acoustic system are very fast and the unstable frequency of the pressure oscillations is high. Examples of A time histories for a stable and for unstable cases are presented in the next section.

For each set of parameters, the simulation is run for 1.0 s, which is enough to reach either saturation to limit-cycle pressure oscillations or zero pressure fluctuations. Additional excitation as shown in Figures 7 and 8 is added to the velocity at the reference position for the first $t_{\mathrm{exc}} = 0.1$ s. The normalized amplitude of the excitation is 1%. In this way, we simulate the noise produced by turbulent combustion. After 0.1 s until 1.0 s, the system is left to evolve by itself without external excitations. The maximum amplitudes of velocity oscillations at the reference position are measured in the window 0.9–1.0 s and plotted. The FFT of the velocity time history is performed and the dominating frequencies of oscillation are reported.

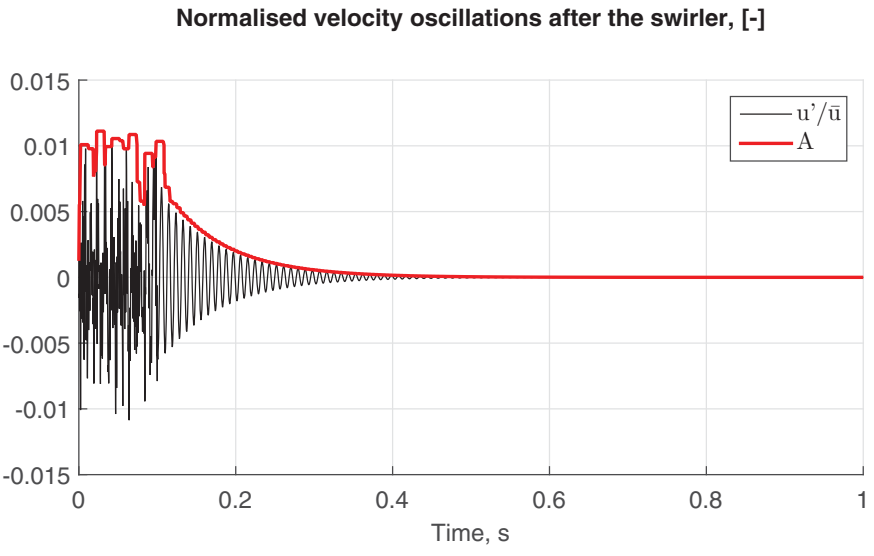

Figure 18. Velocity perturbations at the reference position with $L_{\text{c.c.}} = 0.3$ m. (Colour online)

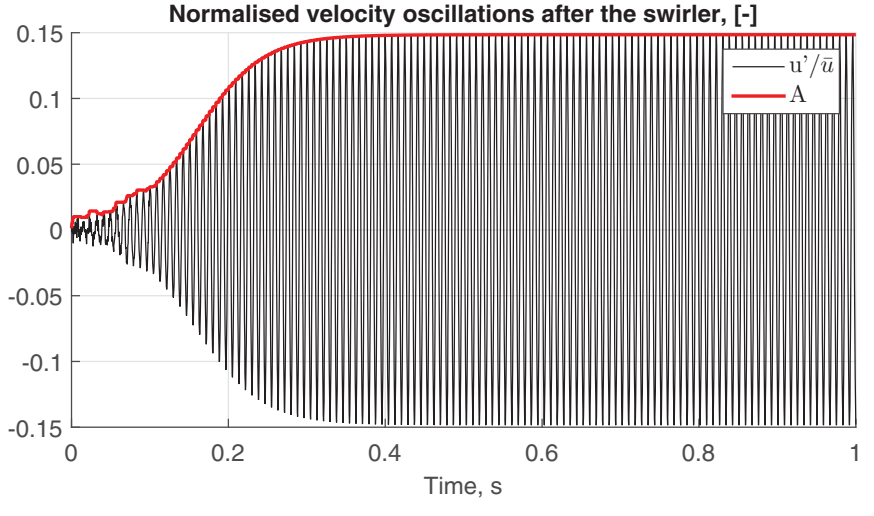

Figure 19. Velocity perturbations at the reference position with $L_{\text{c.c.}} = 0.7$ m. (Colour online)

5.2. *Results of network model simulations*

An unstable frequency at 101.3 Hz was detected in the experiments of Tay-Wo-Chong *et al.* [16] with a combustor length of 0.7 m. With the length of combustor equal to 0.3 m, the set-up was stable [45]. We have performed corresponding simulations and have found that the set-up is stable with a combustion chamber length of $L_{\text{c.c.}} = 0.3$ m (see Figure 18), and with a combustion chamber length of $L_{\text{c.c.}} = 0.7$ m the set-up is unstable (see Figure 19) as in experiments of Tay-Wo-Chong and Polifke [45]. The FFTs of the velocity oscillations for the two cases are shown in Figure 20. In Figure 19 it is possible to see how the nonlinear flame model works: first perturbations grow exponentially and then they saturate to a certain level.

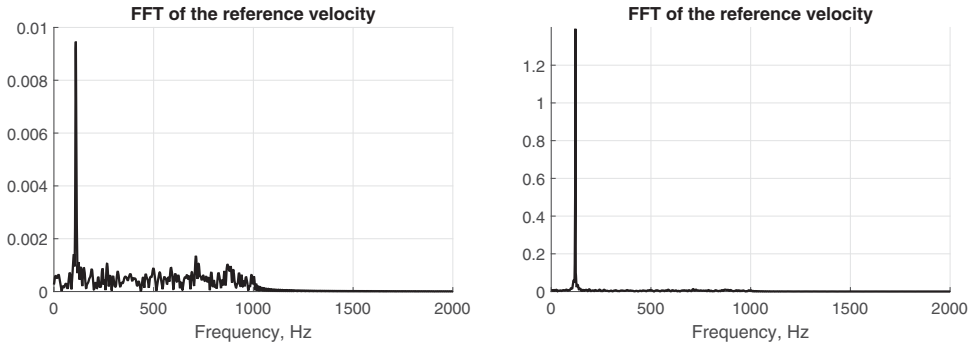

(a) $L_{c.c.} = 0.3$ m. (b) $L_{c.c.} = 0.7$ m.

Figure 20. FFT of velocity perturbations at the reference position.

A parametric study with combustion chamber lengths in the range 0.3–0.95 m in steps of 0.05 m has been performed. With the URANS FDF model used (see Section 4.1), the set-up is predicted to be stable for $L_{\text{c.c.}} = 0.3,\ldots, 0.5$ m and unstable for $L_{\text{c.c.}} = 0.55,\ldots, 0.95$ m (see Figure 21). With the hybrid experimental–URANS FDF model (see Section 4.2) the set-up is predicted to be stable for $L_{\text{c.c.}} = 0.3,\ldots, 0.35$ m and unstable for $L_{\text{c.c.}} = 0.4,\ldots, 0.75$ m (see Figure 21). The saturation amplitude of velocity oscillations at the reference position is higher with the hybrid FDF model due to the higher experimental FTF gain (see Figure 16). Higher saturation amplitudes result in slightly higher unstable frequencies, as explained further. For the $L_{\text{c.c.}}$ values presented in this work, the velocity perturbations saturate at amplitudes lower than 70% – the maximum excitation amplitude used in the FDF calculations. The computed unstable frequency corresponds to the one observed in experiments. Unfortunately, the amplitudes of acoustic oscillations are not available from the experiment.

The following acoustic frequencies are computed in network model simulations without an active flame: 50 and 283 Hz and its harmonics, 956 and 1157 Hz and its harmonics. The first indicated frequency is produced by a Helmholtz resonance of the plenum and the burner tube. The second one corresponds to the quarter-wave mode of the combustor. The third and the last acoustic frequencies are the half-wave modes of the burner tube and of the plenum respectively. The unstable frequency computed with the active flame and reported in Figure 21 does not correspond to any of these frequencies but is the so-called Intrinsic Thermo-Acoustic (ITA) mode [5,49]. The frequency and stability of the ITA mode are influenced by the acoustics of the system as noted by Iurashev *et al.* [50].

Then, the results of linear and weakly nonlinear analyses are compared using the FTF and the FDF computed numerically. In the linear analysis, there is no limit amplitude of acoustic oscillations because they grow (or decay) exponentially. It is possible to calculate the growth rate of velocity fluctuations from time-domain simulations assuming the following law for its development:

$$u'(t) = \sum_{i=1}^{n} U_i \sin(2\pi f_i t + \phi_i) \mathrm{e}^{\alpha_i (t - t_{\text{exc}})}, \tag{18}$$

where f_i is one of the frequencies of pressure oscillations after t_{exc}, n is the number of frequencies of pressure oscillations after t_{exc}, U_i is the amplitude of velocity oscillations at

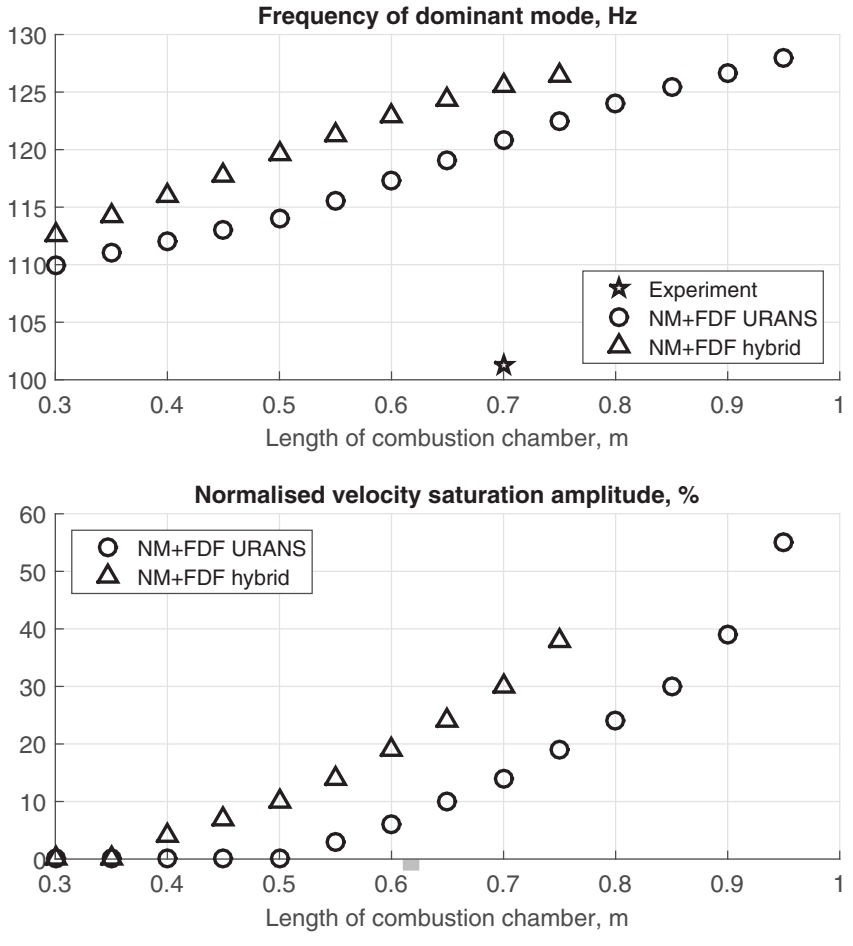

Figure 21. Amplitudes of velocity perturbations at the reference position in network model simulations and their dominant frequencies using two FDFs: the pure URANS FDF model described in Section 4.1 and the hybrid experimental–URANS FDF model described in Section 4.2.

f_i at the time t_{exc}, ϕ_i is the phase of the pressure oscillations at f_i, and α_i is the growth rate of the mode f_i.

The frequencies of oscillations and their growth rates are computed by approximating the time history of pressure oscillations by Equation (18) using the least-squares method. In the simulations presented in this work, either one or no unstable frequency per run is detected, thus $n = 1$ for all simulations in the network model. Positive values of the growth rate parameter α indicate that the system is unstable, and negative values of α mean that the system is stable.

In the case of $L_{\text{c.c.}} = 0.65$ m, when in weakly nonlinear simulation velocity oscillations at the reference position saturate at 10% (see Figure 21), the linear and weakly nonlinear analysis predict the same frequency of oscillations (see Figure 22). In the weakly nonlinear analysis, while increasing stability parameter $L_{\text{c.c.}}$, amplitudes of oscillations grow (see Figure 21), the phase of the FDF changes (see Figure 10) that results in the changing of the frequency of oscillations (see Figure 22). However, in the linear analysis, the phase

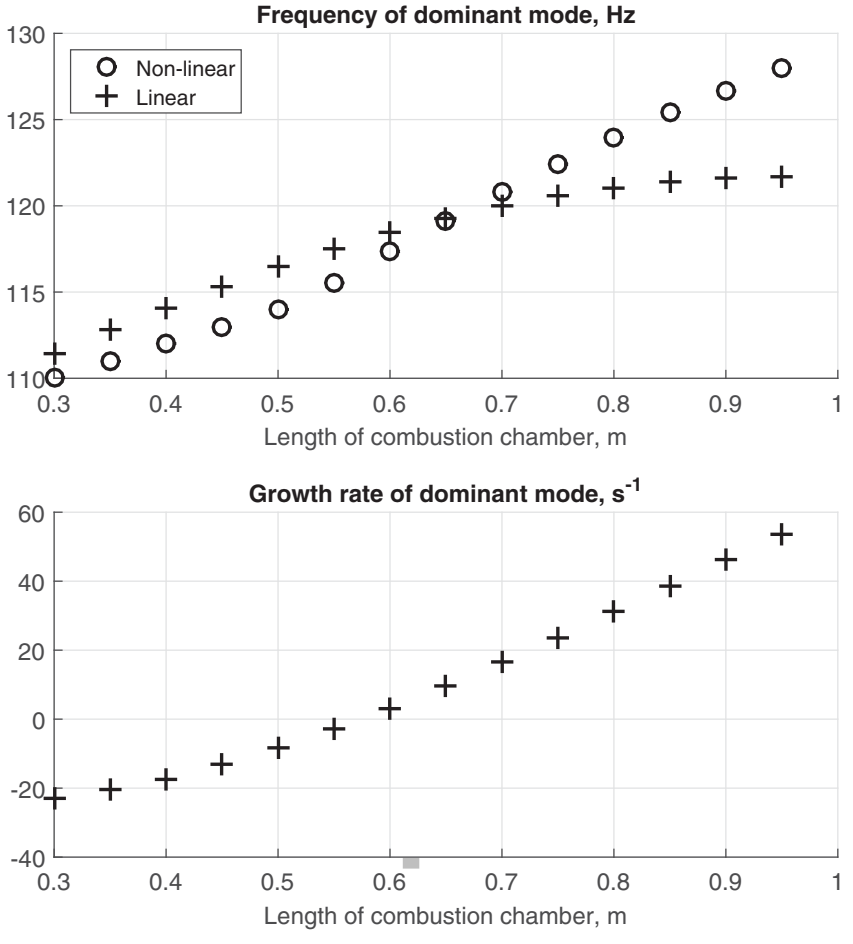

Figure 22. Unstable frequencies of velocity perturbations at the reference position calculated by linear and weakly nonlinear analyses.

of the FTF remains the same and the predicted unstable frequency does not depend on the stability parameter $L_{\text{c.c.}}$. Thus, it is evidenced that if one would like to predict correctly the frequency of the unstable ITA mode, the nonlinear analysis should be performed.

6. Conclusions

In this work, a three-step analysis of combustion instabilities in the time domain has been proposed. The first step consists in obtaining the flame describing function of the system by means of URANS simulations with the FSC model implemented in OpenFOAM®. The FSC model used is extended with respect to the standard one to take into account the effect of heat losses and strain on the flame, which is particularly important for the burner considered. The second step is to approximate the FDF obtained at the first step with an appropriate analytical model. The third step is to perform time-domain simulations using a wave-based approach implemented in Simulink® with the FDF model from the second step.

The main scope of the present work is to show that the number of CFD simulations for the FDF calculation can be reduced if the proposed FDF model is utilized. Thus, the weakly nonlinear analysis of combustion instabilities in gas turbines would require less effort.

This three-step approach has been applied to the BRS test rig and it is shown that the proposed approach can be used successfully for the stability analysis. For conditions when the test rig was unstable in experiments, the proposed stability analysis also predicts the set-up to be unstable. The computed unstable frequency corresponds to the unstable frequency observed in the experiments, which is not a pure acoustic mode of the system but is an intrinsic thermo-acoustic mode. We have shown that if the unstable acoustic perturbations at the ITA frequency saturate at high amplitudes, a nonlinear analysis should be used to predict this frequency correctly.

As a future development of this work, we plan to take into consideration entropy wave propagation, which is important for technically-premixed flames. The approach will be tested on an industrial set-up where amplitudes of pressure oscillations are available. Moreover, implementation of the network model in a Simulink® environment permits the testing of not only passive dampers of undesirable pressure oscillations, such as Helmholtz resonators, but active tools as well (e.g. a controller connected to a siren or an active fuel flow control).

Acknowledgments

Dmytro Iurashev is grateful to Alp Albayrak for familiarizing him with the BRS set-up and for consultation on the OpenFOAM® environment. Assistance from Dr Joel Guerrero with the OpenFOAM® environment is also highly appreciated. The authors would like to acknowledge Professor Maria Heckl for the smooth running of the TANGO project and for many useful discussions. The support of Luis Tay-Wo-Chong with CFD simulations is very much appreciated. Continuous support of this research by Professor Alessandro Bottaro is most gratefully acknowledged.

Disclosure statement

No potential conflict of interest was reported by the authors.

Funding

The presented work is part of the Marie Curie Initial Training Network Thermo-acoustic and Aero-acoustic Nonlinearities in Green combustors with Orifice structures (TANGO). The authors gratefully acknowledge financial support from the European Commission [FP7-PEOPLE-ITN-2012].

References

[1] Y. Huang and V. Yang, *Dynamics and stability of lean-premixed swirl-stabilized combustion*, Prog. Energy Combust. Sci. 35 (2009), pp. 293–364.

[2] T.C. Lieuwen and V. Yang (eds.), *Combustion Instabilities in Gas Turbine Engines: Operational Experience, Fundamental Mechanisms, and Modelling*, Vol. 210 of the series Progress in Astronautics and Aeronautics, American Institute of Astronautics and Aeronautics, Reston, VA, 2005.

[3] W.A. Sirignano, *Driving mechanisms for combustion instability*, Combust. Sci. Technol. 17 (2015), pp. 419–422. Available at https://doi.org/10.1080/00102202.2014.973801.

[4] T. Poinsot and D. Veynante, *Theoretical and Numerical Combustion*, 2nd ed., Edwards, Philadelphia, PA, 2005.

[5] C. Silva, T. Emmert, S. Jaensch, and W. Polifke, *Numerical study on intrinsic thermoacoustic instability of a laminar premixed flame*, Combust. Flame 162(9) (2015), pp. 3370–3378.

[6] E. Courtine, L. Selle, and T. Poinsot, *DNS of intrinsic thermoacoustic modes in laminar premixed flames*, Combust. Flame 162(9) (2015), pp. 4331–4341.
[7] B. Franzelli, E. Riber, L. Gicquel, and T. Poinsot, *Large eddy simulation of combustion instabilities in a lean partially premixed swirled flame*, Combust. Flame 159 (2012), pp. 621–637.
[8] G. Staffelbach, L. Gicquel, G. Boudier, and T. Poinsot, *Large eddy simulation of self-excited azimuthal modes in annular combustors*, Proc. Combust. Inst. 32(2) (2009), pp. 2909–2916.
[9] A. Urbano, L. Selle, G. Staffelbach, B. Cuenot, T. Schmitt, S. Ducruix, and S. Candel, *Exploration of combustion instability triggering using large eddy simulation of a multiple injector liquid rocket engine*, Combust. Flame 169 (2016), pp. 129–140.
[10] X. Han and A.S. Morgans, *Simulation of the flame describing function of a turbulent premixed flame using an open-source LES solver*, Combust. Flame 162(5) (2015), pp. 1778–1792.
[11] X. Han, J. Li, and A.S. Morgans, *Prediction of combustion instability limit cycle oscillations by combining flame describing function simulations with a thermoacoustic network model*, Combust. Flame 162(10) (2015), pp. 3632–3647.
[12] L. Zander, *Numerical analysis of the flame dynamics in a reheat combustor*, M.Sc. thesis, Technical University of Berlin, 2015.
[13] T. Komarek and W. Polifke, *Impact of swirl fluctuations on the flame response of a perfectly premixed swirl burner*, J. Eng. Gas Turbines Power 132 (2010), Article ID 061503. Available at https://doi.org/10.1115/1.4000127.
[14] P. Palies, D. Durox, T. Schuller, and S. Candel, *Nonlinear combustion instability analysis based on the flame describing function applied to turbulent premixed swirling flames*, Combust. Flame 158 (2011), pp. 1980–1991.
[15] B. Ćosić, J.P. Moeck, and C.O. Paschereit, *Nonlinear instability analysis for partially premixed swirl flames*, Combust. Sci. Technol. 186(6) (2014), pp. 713–736.
[16] L. Tay-Wo-Chong, S. Bomberg, A. Ulhaq, T. Komarek, and W. Polifke, *Comparative validation study on identification of premixed flame transfer function*, J. Eng. Gas Turbines Power 134 (2012), Article ID 021502. Available at https://doi.org/10.1115/1.4004183.
[17] H. Krediet, C. Beck, W. Krebs, S. Schimek, C.O. Paschereit, and J. Kok, *Identification of the flame describing function of a premixed swirl flame from LES*, Combust. Sci. Technol. 184 (2012), pp. 888–900.
[18] M. Lauer and W. Polifke, *On the adequacy of chemiluminescence as a measure for heat release in turbulent flames with mixture gradients*, J. Eng. Gas Turbines Power 132 (2010), Article ID 061502. Available at https://doi.org/10.1115/1.4000126.
[19] A. Dowling and Y. Mahmoudi, *Combustion noise*, Proc. Combust. Inst. 35(1) (2015), pp. 65–100.
[20] V. Bellucci, B. Schuermans, D. Nowak, P. Flohr, and C. Paschereit, *Thermoacoustic modelling of a gas turbine combustor equipped with acoustic dampers*. J. Eng. Gas Turbines Power 127 (2005), pp. 372–379.
[21] W. Polifke, *Low-order analysis tools for aero- and thermo-acoustic instabilities*, Presented at the Lecture Series 'Advances in Aero-Acoustics and Thermo-Acoustics', Von Karman Institute for Fluid Dynamics, Rhode-St-Genès, Belgium, 15–19 November 2010. Available at https://www.researchgate.net/publication/255738493_Low-Order_Analysis_Tools_for_Aero-_and_Thermo-Acoustic_Instabilities.
[22] B. Schuermans, F. Guethe, D. Pennell, D. Guyot, and C. Paschereit, *Thermoacoustic modelling of a gas turbine using transfer functions measured under full engine pressure*, J. Eng. Gas Turbines Power 132 (2010), Article ID 111503. Available at https://doi.org/10.1115/1.4000854.
[23] M. Bothien, N. Noiray, and B. Schuermans, *Analysis of azimuthal thermo-acoustic modes in annular gas turbine combustion chambers*, J. Eng. Gas Turbines Power 137 (2015), Article ID 061505. Available at https://doi.org/10.1115/1.4028718.
[24] B. Schuermans, W. Polifke, C. Paschereit, and J. van der Linden, *Prediction of acoustic pressure spectra in combustion systems using swirl stabilized gas turbine burners*, in *Proceedings of ASME Turbo Expo 2000: Power for Land, Sea, and Air (IGTI TE2000)*, 8–11 May 2000, Munich, ASME Paper No. 2000-GT-0105. Available at https://doi.org/10.1115/2000-GT-0105.
[25] M.A. Heckl, *Analytical model of nonlinear thermo-acoustic effects in a matrix burner*, J. Sound Vibration 332 (2013), pp. 4021–4036.
[26] K. Kim, J. Lee, B. Quay, and D. Santavica, *Spatially distributed flame transfer functions for predicting combustion dynamics in lean premixed gas turbine combustors*, Combust. Flame 157 (2010), pp. 1718–1730.

[27] S.M. Camporeale, B. Fortunato, and G. Campa, *A finite element method for three-dimensional analysis of thermoacoustic combustion instability*, J. Eng. Gas Turbines Power 133 (1) (2011), Article ID 011506. Available at https://doi.org/10.1115/1.4000606.

[28] M. Schulze, T. Hummel, N. Klarmann, F. Berger, B. Schuermans, and T. Sattelmayer, *Linearized Euler equations for the prediction of linear high-frequency stability in gas turbine combustors*, in *Proceedings of ASME Turbo Expo 2016: Turbomachinery Technical Conference and Exposition*, 13–17 June 2016, Seoul, South Korea, ASME Paper No. GT2016-57818. Available at https://doi.org/10.1115/GT2016-57818.

[29] J. Gikadi, *Prediction of acoustic modes in combustors using linearized Navier–Stokes equations in frequency space*, Ph.D. thesis, Technical University of Munich, Garching, Germany, 2014.

[30] F. Nicoud, L. Benoit, C. Sensiau, and T. Poinsot, *Acoustic modes in combustors with complex impedances and multidimensional active flames*, AIAA J. 45(2) (2007), pp. 426–441.

[31] C. Pankiewitz and T. Sattelmayer, *Time domain simulation of combustion instabilities in annular combustors*, J. Eng. Gas Turbines Power 123(3) (2003), pp. 677–685.

[32] J. Li and A.S. Morgans, *Time domain simulations of nonlinear thermoacoustic behaviour in a simple combustor using a wave-based approach*, J. Sound Vibration 346 (2015), pp. 345–360.

[33] C. Silva, F. Nicoud, T. Schuller, D. Durox, and S. Candel, *Combining a Helmholtz solver with the flame describing function to assess combustion instability in a premixed swirled combustor*, Combust. Flame 160 (2013), pp. 1743–1754.

[34] A.N. Lipatnikov and J. Chomiak, *Turbulent flame speed and thickness: Phenomenology, evaluation, and application in multi-dimensional simulations*, Prog. Energy Combust. Sci. 28 (2002), pp. 1–74.

[35] D. Iurashev, G. Campa, V. Anisimov, A. Di Vita, E. Cosatto, F. Daccà, and A. Albayrak, *Turbulent flame models for prediction of pressure oscillations in gas turbine burners*, in *Proceedings of the 22nd International Congress on Sound and Vibration*, Florence, Italy, 12–16 July 2015.

[36] L. Davidson, *Lecture notes on fluid mechanics, turbulent flow and turbulence modeling*, International Master's Programme in Applied Mechanics, Chalmers University, Sweden, 2016. Available at http://www.tfd.chalmers.se/lada/postscript_files/solids-and-fluids_turbulent-flow_turbulence-modelling.pdf.

[37] L. Tay-Wo-Chong, M. Zellhuber, T. Komarek, H. Im, and W. Polifke, *Combined influence of strain and heat loss on turbulent premixed flame stabilization*, Flow Turbul. Combust. 97(1) (2016), pp. 263–294.

[38] K. Kim, J. Lee, B. Quay, and D. Santavicca, *Spatially distributed flame transfer functions for predicting combustion dynamics in lean premixed gas turbine combustors*, Combust. Flame 157(9) (2011), pp. 1718–1730.

[39] L. Rofi, G. Campa, V. Anisimov, F. Daccá, E. Bertolotto, E. Gottardo, and F. Bonzani, *Numerical procedure for the investigation of combustion dynamics in industrial gas turbines: LES, RANS and thermoacoustics*, in *ASME Turbo Expo 2015: Turbine Technical Conference and Exposition*, 15–19 June 2015, Montreal, Québec, Canada, ASME Paper No. GT2015–42168. Available at https://doi.org/10.1115/GT2015-42168.

[40] T. Schuller, S. Ducruix, D. Durox, and S. Candel, *Modelling tools for the prediction of premixed flame transfer functions*, Proc. Combust. Inst. 29 (2002), pp. 107–113.

[41] V.P. Karpov, A.N. Lipatnikov, and V.L. Zimont, *A model of premixed turbulent combustion and its validation*, Archiv. Combust. 14 (1994), pp. 125–141. Available at http://archcomb.itc.pw.edu.pl/volume-14-no-3-4-1994/a-model-of-premixed-turbulent-combustion-and-its-validation-pp-125-142.

[42] OpenFOAM version 2.3.0, 5 February 2014, User Guide; software available at http://cfd.direct/openfoam/user-guide/.

[43] W. Polifke, A. Poncet, C.O. Paschereit, and K. Doebbeling, *Reconstruction of acoustic transfer matrices by instationary computational fluid dynamics*, J. Sound Vibration 245 (3) (2001), pp. 483–510. Available at https://doi.org/10.1006/jsvi.2001.3594.

[44] A.P. Dowling and S.R. Stow, *Acoustic analysis of gas turbine combustors*, in *Combustion Instabilities in Gas Turbine Engines*, T.C. Lieuwen and V. Yang, eds., Vol. 210 of the series Progress in Astronautics and Aeronautics, American Institute of Astronautics and Aeronautics, Reston, VA, 2005, pp. 369–414.

[45] L. Tay-Wo-Chong and W. Polifke, *Large eddy simulation-based study of the influence of thermal boundary condition and combustor confinement on premix flame transfer functions*, J. Eng. Gas Turbines Power 135 (2013), Article ID 021502. Available at https://doi.org/10.1115/1.4007734.

[46] B.E. Launder, G.J. Reece, and W. Rodi, *Progress in the development of a Reynolds-stress turbulence closure*, J. Fluid Mech. 68(3) (1975), pp. 537–566.
[47] T.J. Poinsot and S.K. Lele, *Boundary conditions for direct simulations of compressible viscous flows*, J. Comput. Phys. 101 (1992), pp. 104–129.
[48] I.E. Idelchik, *Handbook of Hydraulic Resistance*, 3rd ed., Mashinostroienie, Moscow, 1992 (in Russian).
[49] S. Bomberg, T. Emmert, and W. Polifke, *Thermal versus acoustic response of velocity sensitive premixed flames*, Proc. Combust. Inst. 35(3) (2015), pp. 3185–3192.
[50] D. Iurashev, G. Campa, V.V. Anisimov, and E. Cosatto, *Two-step approach for pressure oscillations prediction in gas turbine combustion chambers*, Int. J. Spray Combust. Dynam. Available at https://doi.org/10.1177/1756827717711016.

Appendix A. *Matrices for jump conditions between network model sections*

Matrices for jump conditions between sections for the case of area decrease [44] are

$$\mathbf{F}_{\text{decr}} = \begin{bmatrix} \dfrac{S_d}{\bar{c}_{s,d}}(1+M_d) & \dfrac{S_u}{\bar{c}_{s,u}}(1-M_u) \\ \dfrac{1}{\bar{\rho}_d}[1+M_d(1+\zeta_{\text{decr}})] & -\dfrac{1}{\bar{\rho}_u}(1-M_u) \end{bmatrix},$$

$$\mathbf{K}_{\text{decr}} = \begin{bmatrix} \dfrac{S_u}{\bar{c}_{s,u}}(1+M_u) & \dfrac{S_d}{\bar{c}_{s,d}}(1-M_d) \\ \dfrac{1}{\bar{\rho}_u}(1+M_u) & -\dfrac{1}{\bar{\rho}_d}[1-M_d(1+\zeta_{\text{decr}})] \end{bmatrix},$$

where S is the cross-sectional area, M is the mean Mach number, and ζ is the coefficient of pressure losses.

Matrices for jump conditions between sections for the case of area increase [44] are

$$\mathbf{F}_{\text{incr}} = \begin{bmatrix} \dfrac{S_d}{\bar{c}_{s,d}}(1+M_d) & \dfrac{S_u}{\bar{c}_{s,u}}(1-M_u) \\ \dfrac{1}{\bar{\rho}_d}(1+M_d) & -\dfrac{1}{\bar{\rho}_u}[1-M_u(1-\zeta_{\text{incr}})] \end{bmatrix},$$

$$\mathbf{K}_{\text{incr}} = \begin{bmatrix} \dfrac{S_u}{\bar{c}_{s,u}}(1+M_u) & \dfrac{S_d}{\bar{c}_{s,d}}(1-M_d) \\ \dfrac{1}{\bar{\rho}_u}[1+M_u(1-\zeta_{\text{incr}})] & -\dfrac{1}{\bar{\rho}_d}(1-M_d) \end{bmatrix}.$$

Matrices for jump conditions between sections for the case of temperature jump with active flame and constant cross-sectional area [44] are

$$\mathbf{J} = \begin{bmatrix} (1+2M_d+M_d^2) & -(1-2M_u+M_u^2) \\ \left[\dfrac{\bar{c}_s+\gamma\bar{u}}{\gamma-1}+\dfrac{3\bar{u}^2}{2\bar{c}_s}+\dfrac{\bar{u}^3}{2\bar{c}_s^2}\right]_d & -\left[\dfrac{\bar{c}_s-\gamma\bar{u}}{\gamma-1}+\dfrac{3\bar{u}^2}{2\bar{c}_s}-\dfrac{\bar{u}^3}{2\bar{c}_s^2}\right]_u \end{bmatrix},$$

$$\mathbf{H} = \begin{bmatrix} (1+2M_u+M_u^2) & -(1-2M_d+M_d^2) & 0 \\ \left[\dfrac{\bar{c}_s+\gamma\bar{u}}{\gamma-1}+\dfrac{3\bar{u}^2}{2\bar{c}_s}+\dfrac{\bar{u}^3}{2\bar{c}_s^2}\right]_u & -\left[\dfrac{\bar{c}_s-\gamma\bar{u}}{\gamma-1}+\dfrac{3\bar{u}^2}{2\bar{c}_s}-\dfrac{\bar{u}^3}{2\bar{c}_s^2}\right]_d & \dfrac{1}{S} \end{bmatrix},$$

where γ is the heat capacity ratio.